CELL BIOLOGY

The nucleus acts as a ruler tailoring cell responses to spatial constraints

A. J. Lomakin*†‡, C. J. Cattin†, D. Cuvelier§, Z. Alraies§, M. Molina, G. P. F. Nader, N. Srivastava, P. J. Sáez, J. M. Garcia-Arcos, I. Y. Zhitnyak, A. Bhargava, M. K. Driscoll, E. S. Welf, R. Fiolka, R. J. Petrie, N. S. De Silva, J. M. González-Granado, N. Manel, A. M. Lennon-Duménil, D. J. Müller*, M. Piel*‡

INTRODUCTION: The human body is a crowded place. This crowding is even more acute when the regulation of cell growth and proliferation fails during the formation of a tumor. Dealing with the lack of space in crowded environments presents cells with a challenge. This is especially true for immune cells, whose task is to patrol tissues, causing them to experience both acute and sustained deformation as they move. Although changes in tissue crowding and associated cell shape alterations have been known by pathologists to be key diagnostic traits of late-stage tumors since the 19th century, the impact of these changes on the biology of cancer and immune cells remains unclear. Moreover, it is not known whether cells can detect and adaptively respond to deformations in densely packed spaces.

RATIONALE: To test the hypothesis that cells possess an ability to detect and respond to environmentally induced changes in their shape, we fabricated artificial microenvironments that mimic the conditions experienced by tumor and immune cells in a crowded tissue. By combining dynamic confinement, force measurements, and live cell imaging, we were able to quantify cell responses to precisely controlled physical perturbations of their shape.

RESULTS: Our results show that, although cells are surprisingly resistant to compressive forces, they monitor their own shape and develop an active contractile response when deformed below a specific height. Notably, we find that this is achieved by cells monitoring the deformation of their largest internal compartment: the nucleus. We establish that the nucleus provides cells with a precise measure of the extent of their deformation. Once cell compression exceeds the size of the nucleus, it causes the bounding nuclear envelope (NE) to unfold and stretch. The onset of the contractile response occurs when the NE reaches a fully unfolded state. This transition in the mechanical state of the NE and its membranes permits calcium release from internal membrane stores and activates the calcium-dependent phospholipase cPLA2, an enzyme known to operate as a molecular sensor of nuclear membrane tension and a critical regulator of signaling and metabolism. Activated cPLA2 catalyzes the formation of arachidonic acid, an omega-6 fatty acid that, among other processes, potentiates the adenosine triphosphatase activity of myosin II. This induces contractility of the actomyosin cortex, which produces pushing forces to resist physical compression and to rapidly squeeze the cell out of its compressive microenvironment in an "evasion reflex" mechanism.

CONCLUSION: Although the nucleus has traditionally been considered a passive storehouse for genetic material, our work identifies it as an active compartment that rapidly convers mechanical inputs into signaling outputs, with a critical role of its envelope in this sensing function. The nucleus is able to detect environmentally imposed compression and respond to it by generating a signal that is used to change cell behaviors. This phenomenon plays a critical role in ensuring that cells, such as the immune cells within a tumor, can adapt, survive, and efficiently move through a crowded and mechanically heterogeneous microenvironment. Characterizing the full spectrum of signals triggered by nuclear compression has the potential to elucidate mechanisms underlying signaling, epigenetic, and metabolic adaptations of cells to their mechanoenvironment and is thus an exciting avenue for future research. ∎

S READ THE FULL ARTICLE AT
https://doi.org/10.1126/science.aba2894

The nuclear ruler and its contribution to the "life cycle" of a confined cell.
(1) Cell confinement below resting nucleus size, leading to nuclear deformation and to unfolding, and stretching of the nuclear envelope.
(2) Nuclear membrane tension increase, which triggers calcium release, cPLA2 activation, and arachidonic acid (ARA) production. (3) Actomyosin force (F) generation. (4) Increased cell migratory capacity and escape from confinement.

2 Nuclear membrane stretch
cPLA2 OFF
cPLA2 ON
Ca^{2+}
Ca^{2+}
Ca^{2+}
ARA
1 Cell confinement below resting nucleus diameter
3 Cortical actomyosin contractility
F
4 Rapid evasion of mechanically-restrictive environments
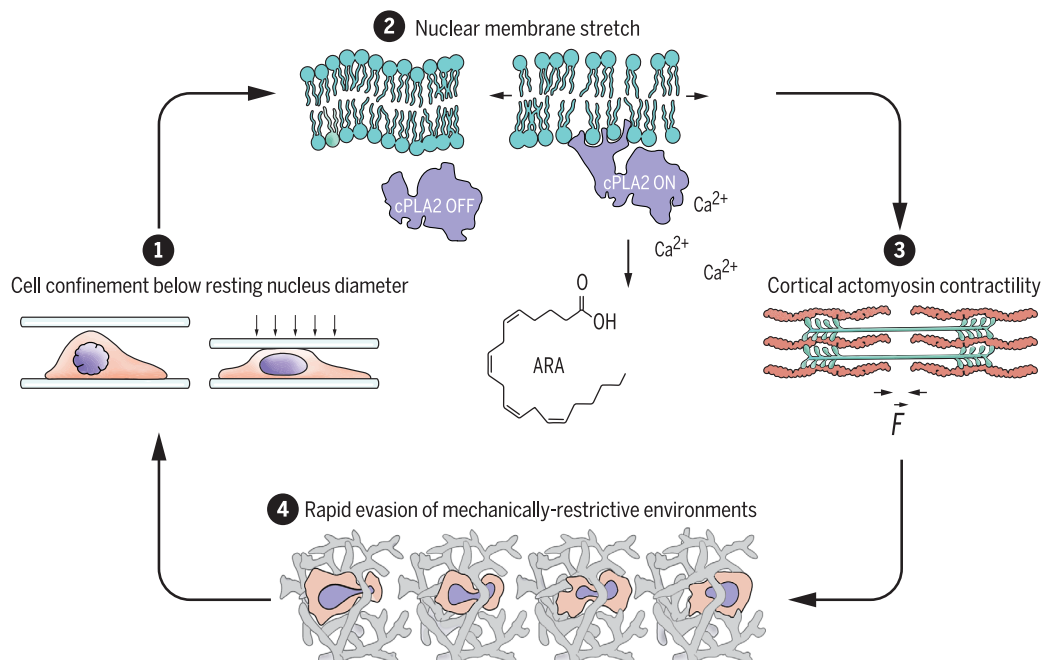
RESEARCH ARTICLE

CELL BIOLOGY

The nucleus acts as a ruler tailoring cell responses to spatial constraints

A. J. Lomakin[1,2,3,4,5,6]*†‡, C. J. Cattin[7]†§, D. Cuvelier[6,8]¶, Z. Alraies[6,8,9]¶, M. Molina[5]#,
G. P. F. Nader[6,8], N. Srivastava[6,8], P. J. Sáez[6,8]**, J. M. Garcia-Arcos[6,8], I. Y. Zhitnyak[6,8,10],
A. Bhargava[9], M. K. Driscoll[11,12], E. S. Welf[11,12], R. Fiolka[11,12], R. J. Petrie[13], N. S. De Silva[9],
J. M. González-Granado[14,15], N. Manel[9], A. M. Lennon-Duménil[9], D. J. Müller[7]*, M. Piel[6,8]*‡

The microscopic environment inside a metazoan organism is highly crowded. Whether individual cells can tailor their behavior to the limited space remains unclear. In this study, we found that cells measure the degree of spatial confinement by using their largest and stiffest organelle, the nucleus. Cell confinement below a resting nucleus size deforms the nucleus, which expands and stretches its envelope. This activates signaling to the actomyosin cortex via nuclear envelope stretch-sensitive proteins, up-regulating cell contractility. We established that the tailored contractile response constitutes a nuclear ruler–based signaling pathway involved in migratory cell behaviors. Cells rely on the nuclear ruler to modulate the motive force that enables their passage through restrictive pores in complex three-dimensional environments, a process relevant to cancer cell invasion, immune responses, and embryonic development.

Much like modern-day engineered devices, cells in the human body are able to make measurements. For example, epithelial cells in the intestine monitor local cell densities and exit the tissue above a threshold density, preventing hyperplasia (1). Immune cells can estimate the pore size of surrounding tissues to choose the site of least mechanical resistance for migration (2). Epidermal stem cells use the amount of extracellular matrix (ECM) available for cell attachment and spreading as a guidance cue in their cell fate decision-making (3). These examples illustrate the sensitivity of complex cell behaviors to environmental spatial and mechanical constraints, known in quantitative sciences as boundary conditions (BCs) (4). Although the importance of BCs in cell physiology is increasingly recognized, only a few mechanisms by which cells can measure specific BCs are precisely identified [e.g., the stiffness of the substrate on which cells grow (5) or the geometry of their adhesive environment (6)]. Among the known mechanisms, most are related to either strain (deformation) or stress (forces) and are collectively referred to as mechanotransduction pathways (7).

In this study, we investigated whether cells are also equipped with a mechanism to measure absolute dimensions, which could inform them about distances between neighboring cells or matrix pore size. In our previous study, we discovered that many histologically unrelated cell types change their migratory strategies in response to the specific confinement height (8). This almost universally leads to a long-lasting increase in actomyosin contractility and amoeboid cell propulsion in the absence of specific adhesion to the substrate. Together with similar findings in early zebrafish embryos (9), these observations illustrate the simplest case in which cells measure one of their dimensions to adapt their behavior to local BCs in vitro and in vivo. However, the mechanism underlying this phenomenon remained unknown.

Cells detect their height and trigger contractile responses below a threshold height

To elucidate the mechanism by which cells measure their dimensions, we applied a reductionist approach in which the degree of cell confinement is precisely controlled and paralleled with quantitative microscopy. We confined single nonadherent, initially rounded, interphase cells by using an ion beam–sculpted flat silicon microcantilever (Fig. 1A) mounted on an atomic force microscopy (AFM) setup (10) and simultaneously monitored the actomyosin cytoskeleton dynamics and contractile force generation by employing confocal videomicroscopy and AFM-based force spectroscopy.

Using the cell line HeLa-Kyoto (human cervical carcinoma) that expresses MYH9-GFP (myosin IIA), we performed confinement experiments in which the height of the same single cell is changed in a stepwise fashion, starting from 20 μm (average nonconfined cell diameter is 20 ± 4 μm, n = 100 cells). We found that upon reaching a specific confinement height, cells begin responding by steadily increasing the force with which they push against the confining cantilever (6- to 5-μm confinement in Fig. 1A). Each cell had its own trigger height at which it generated the force response (Fig. 1A, right graph). Most cells remained insensitive to 10-μm confinement (which corresponds to half of the initial cell height; Fig. 1B), whereas almost 100% of analyzed cells displayed the response upon reaching 5-μm confinement (Fig. 1A, right graph). We thus chose to systematically study the response of cells to 5- versus 10-μm confinement height.

Our analyses showed that cell confinement to 5 μm, but not 10 μm, stimulates rapid (2.05 ± 0.33 min, n = 10 cells) recruitment of myosin II (hereafter referred to as myosin) from the cytosol to the cortex (Fig. 1, C and D, fig. S1A, and movie S1), followed by cell cortex contraction and force production (Fig. 1E). Both phenomena required myosin activity (Fig. 1, D and E) and culminated in a sustained (up to several hours) and active nonapoptotic plasma membrane (PM) blebbing (movie S2), whose degree is directly proportional to cortical myosin concentration (fig. S1, B to D). Measuring cell blebbing index in several other primary and immortalized cell lines under different confinement heights confirmed the generality of our observations (fig. S1E). To test whether cells would also adapt their cortical actomyosin contractility to the degree of environmental confinement in a context that more closely recapitulates in vivo settings, we examined human fibrosarcoma cells HT1080 infiltrating three-dimensional (3D) cell-derived matrices (CDMs) (Fig. 1F). Cortical recruitment of myosin in these cells linearly scaled with the self-imposed smallest dimension of the cell (Fig. 1F), thus validating our AFM-based observations. Notably, switching cells back to the initial unconfined state in our AFM experiments induced a rapid (3.78 ± 0.94 min, n = 7 cells) relocalization of myosin to the cytosol (fig. S1F), indicating that persistent contractility required a sustained

[1]St. Anna Children's Cancer Research Institute (CCRI), Vienna, Austria. [2]Ludwig Boltzmann Institute for Rare and Undiagnosed Diseases (LBI-RUD), Vienna, Austria. [3]CeMM Research Center for Molecular Medicine, Austrian Academy of Sciences (ÖAW), Vienna, Austria. [4]Medical University of Vienna (MUV), Vienna, Austria. [5]Centre for Stem Cells and Regenerative Medicine, School of Basic and Medical Biosciences, King's College London, London, UK. [6]Institut Curie, PSL Research University, CNRS, UMR 144, Paris, France. [7]Department of Biosystems Science and Engineering, ETH Zurich, Basel, Switzerland. [8]Institut Pierre Gilles de Gennes, PSL Research University, Paris, France. [9]Institut Curie, PSL Research University, INSERM, U 932, Paris, France. [10]N.N. Blokhin Medical Research Center of Oncology, Moscow, Russia. [11]Department of Cell Biology, University of Texas Southwestern Medical Center, Dallas, TX, USA. [12]Lyda Hill Department of Bioinformatics, University of Texas Southwestern Medical Center, Dallas, TX, USA. [13]Department of Biology, Drexel University, Philadelphia, PA, USA. [14]LamImSys Lab, Departamento de Fisiología, Facultad de Medicina, Universidad Autónoma de Madrid (UAM), Madrid, Spain. [15]Instituto de Investigación Hospital 12 de Octubre (imas12), Madrid, Spain.
*Corresponding author. Email: alexis.lomakin@ccri.at, alexis.lomakin@meduniwien.ac.at (A.J.L.); daniel.mueller@bsse.ethz.ch (D.J.M.); matthieu.piel@curie.fr (M.P.)
†These authors contributed equally to this work.
‡These authors contributed equally to this work.
§Present address: F. Hoffmann-La Roche Ltd., Basel, Switzerland.
¶These authors contributed equally to this work.
#Present address: Institute for Bioengineering of Catalonia (IBEC), Barcelona Institute of Science and Technology (BIST) and University of Barcelona, Barcelona, Spain.
**Present address: Department of Biochemistry and Molecular Cell Biology, University Medical Center Hamburg-Eppendorf, Hamburg, Germany.

Fig. 1. Cells sense their own height and up-regulate actomyosin contractility at a specific height. (**A**) (Left) Representative force curve in response to stepwise (1-μm increment, 5-min interval) confinement of a cell by the flat microcantilever. (Right) Percentage of cells displaying a sustained force increase (>15 nN) as a function of height. (**B**) 3D images (*xz* views) of the same live HeLa-Kyoto cell expressing MYH9-GFP at indicated heights (*h*). (**C**) Time-lapse image sequence of the same live cell (*xy* views; single, midplane, confocal slices) at 10 μm (top), followed by a height change to 5 μm (bottom). Scale bar, 10 μm. (**D**) (Left) Representative graph of myosin cortex-to-cytoplasm ratio as a function of time in the same live cell upon 10-μm and subsequently 5-μm confinement. (Middle and right) The same ratio measured in single live cells at 10-μm and subsequently 5-μm confinement in the presence of DMSO or the ROCK inhibitor Y27632 (*n* = 10 cells per condition; *P* value, paired *t* test). Measurements were taken 5 min after application of each confinement height. (**E**) (Left) Representative force response curve (Δ*F*, force increase) as a function of time in the same live cell upon 10-μm and subsequently 5-μm confinement. (Middle) Statistical analysis of force response (Δ*F*) in cells at 10 versus 5 μm. (Right) Statistical analysis of force response (Δ*F*) to 5-μm confinement in cells treated with DMSO or Y27632. Measurements were taken 5 min after application of the confinement. Data are from ≥2 experiments (mean ± SD; *n* = 10 cells per condition; *P* value, unpaired *t* test). (**F**) (Left) Representative image of 3D dermal fibroblast CDM stained with a collagen I antibody. (Middle) Representative images of HT1080 cells expressing GFP-myosin light chain 2 (GFP-MLC2) in 3D CDM (*xy* views, single confocal slices) with the smallest cell dimension (*h*) measured as 10 and 5 μm. (Right) Self-imposed smallest cell dimensions plotted against corresponding values for myosin cortex-to-cytoplasm ratio in the cells within 3D CDM (*n* = 30 cells). Scale bar, 20 μm.
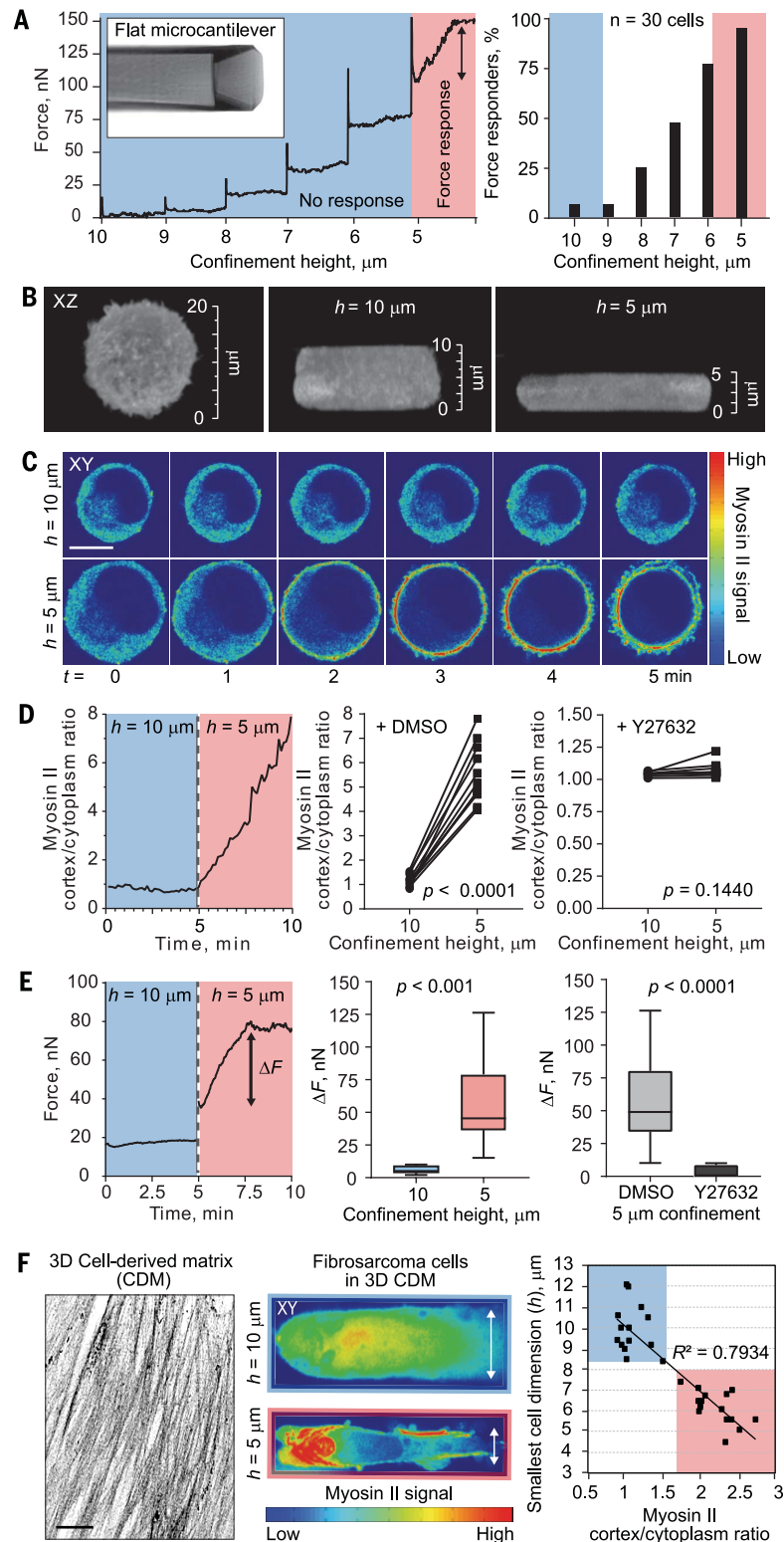
confinement below the threshold height. Collectively, these experiments showed that single cells can sense the difference between 10 and 5 μm and can trigger a sustained, yet reversible, active contractile response at a specific height.

Cell height–specific contractile responses depend on nuclear envelope– and/or endoplasmic reticulum–mediated signals

We next performed experiments to narrow the range of potential mechanisms involved in this height-dependent contractile response.

Confinement experiments on adherent, well-spread cells showed qualitatively the same threshold-like response as we established for rounded nonadherent cells (fig. S2, A to C). Moreover, experimental manipulations of extracellular [Ca²⁺] or [Mn²⁺] to modulate
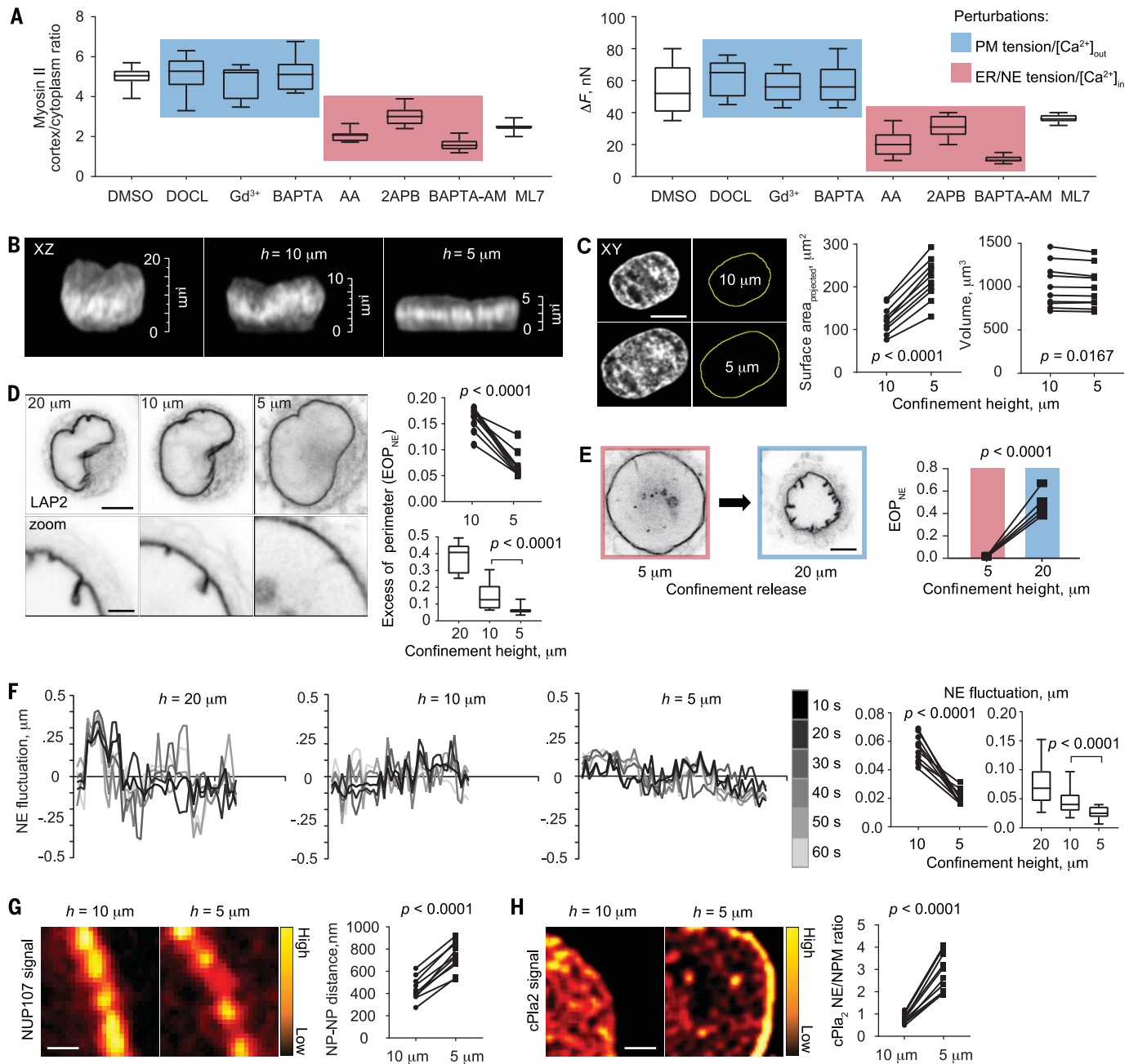
Fig. 2. The height-specific contractile response is controlled by mechanisms associated with nuclear–ER membrane stretch. (**A**) Cortical myosin levels (left) and force response (ΔF; right) to 5-μm confinement of HeLa-Kyoto cells treated with drugs affecting PM tension and extracellular $[Ca^{2+}]_{out}$ (blue) or ER-NE tension and intracellular $[Ca^{2+}]_{in}$ (red). See table S1 for drug target description and materials and methods for drug concentrations. Data are from ≥2 experiments (mean ± SD; $n = 10$ cells per perturbation; see table S2 for statistics). (**B**) 3D xz views of the DAPI-stained nucleus at 20, 10, and 5 μm. (**C**) (Left) xy views of the nucleus at 10 and 5 μm. (Middle and right) Measurements of nuclear area and volume at 10 μm and subsequently 5 μm ($n = 10$ cells; P value, paired t test). Scale bar, 10 μm. (**D**) (Left top) Images of the LAP2-GFP–labeled NE confined to 20, 10, and 5 μm. Scale bar, 5 μm. (Left bottom) Zoomed-in view of a gradually opening nuclear fold. Scale bar, 2.5 μm. (Right) EOP$_{NE}$ at 10 μm and subsequently 5 μm (upper

graph, $n = 10$ different cells; P value, paired t test) and statistics of EOP$_{NE}$ in cell populations at 20, 10, and 5 μm (lower graph, data are from ≥2 experiments; mean ± SD; $n = 30$ cells per height; P value, unpaired t test). (**E**) Images of the LAP2-GFP–labeled NE and EOP$_{NE}$ quantifications in live cells confined to 5 μm and unconfined to 20 μm ($n = 10$ cells; P value, paired t test). Scale bar, 5 μm. (**F**) NE fluctuation curves at various confinement heights (h) and quantifications of NE fluctuations at 10 and subsequently 5 μm ($n = 10$ cells; P value, paired t test) or in cell populations at 20, 10, and 5 μm (mean ± SD; $n = 30$ cells per height; P value, unpaired t test). (**G**) Images of NUP107–GFP-labeled nuclear pores (NPs) and quantification of inter-NP (NP-NP) distance at 10 and subsequently 5 μm ($n = 10$ cells; P value, paired t test). Scale bar, 0.5 μm. (**H**) Images of nuclear cPla2-mKate2 signal and quantification of its NE-to-nucleoplasm (NE/NPM) ratio at 10 and subsequently 5 μm ($n = 10$ cells; P value, paired t test). Scale bar, 1.5 μm.

engagement of integrins during cell contact with the surface of the confining cantilever (*11*) did not affect the response in nonadherent suspended cells (fig. S2D). This suggested that the sensing mechanism does not depend on classical integrin-based mechanotransduction pathways. The sustained increase in contractility (fig. S1D), and the fact that the response was dependent on the confinement height per se rather than the speed of confinement (fig. S3), renders unlikely a signal originating from strain in the actin cortex or the PM, because these structures dissipate stress in minutes as a result of fast turnover (*12*). A natural candidate that matches the range of relevant confinement heights at which the response is triggered and that can display long-term stress due to slow turnover of its stiff elastic shell is

the cell nucleus (*13*). Indeed, the nucleus, and more specifically its envelope, has been shown in the recent years to trigger diverse cell responses when the nuclear compartment is deformed: entry of the transcription factors YAP/TAZ (*14*), activation of the ATR kinase (*15*), release of calcium (*16*), activation of the calcium-dependent phospholipase cPLA2 (*17*), and nuclear envelope (NE) rupture accompanied by DNA damage (*18*). Considering that the response to confinement was reversible and required only a few minutes for its manifestation, potential changes at the level of cell transcription and translation are not likely, and we confirmed this experimentally by acutely inhibiting the processes of transcription and translation (fig. S4A). Blocking the ATR kinase activity did not yield a pheno-

type either (fig. S4B). Moreover, ruptures of neither the NE nor the PM were observed at 5-μm confinement (fig. S4, C and D), excluding a mechanism based on an extracellular signal influx through transient holes in the PM or mixing of cytoplasmic and nuclear contents.

We thus performed a small pharmacological inhibitors screen, targeting mechanotransductive pathways compatible with a cellular confinement response on a time scale of minutes (table S1). The screen (Fig. 2A and table S2) showed that extracellular calcium, PM-associated stretch-sensitive channels, and PM tension are not involved in the response to confinement. However, intracellular calcium, intracellular stretch-sensitive calcium channels associated with the perinuclear endoplasmic reticulum (ER), the calcium-dependent myosin light chain
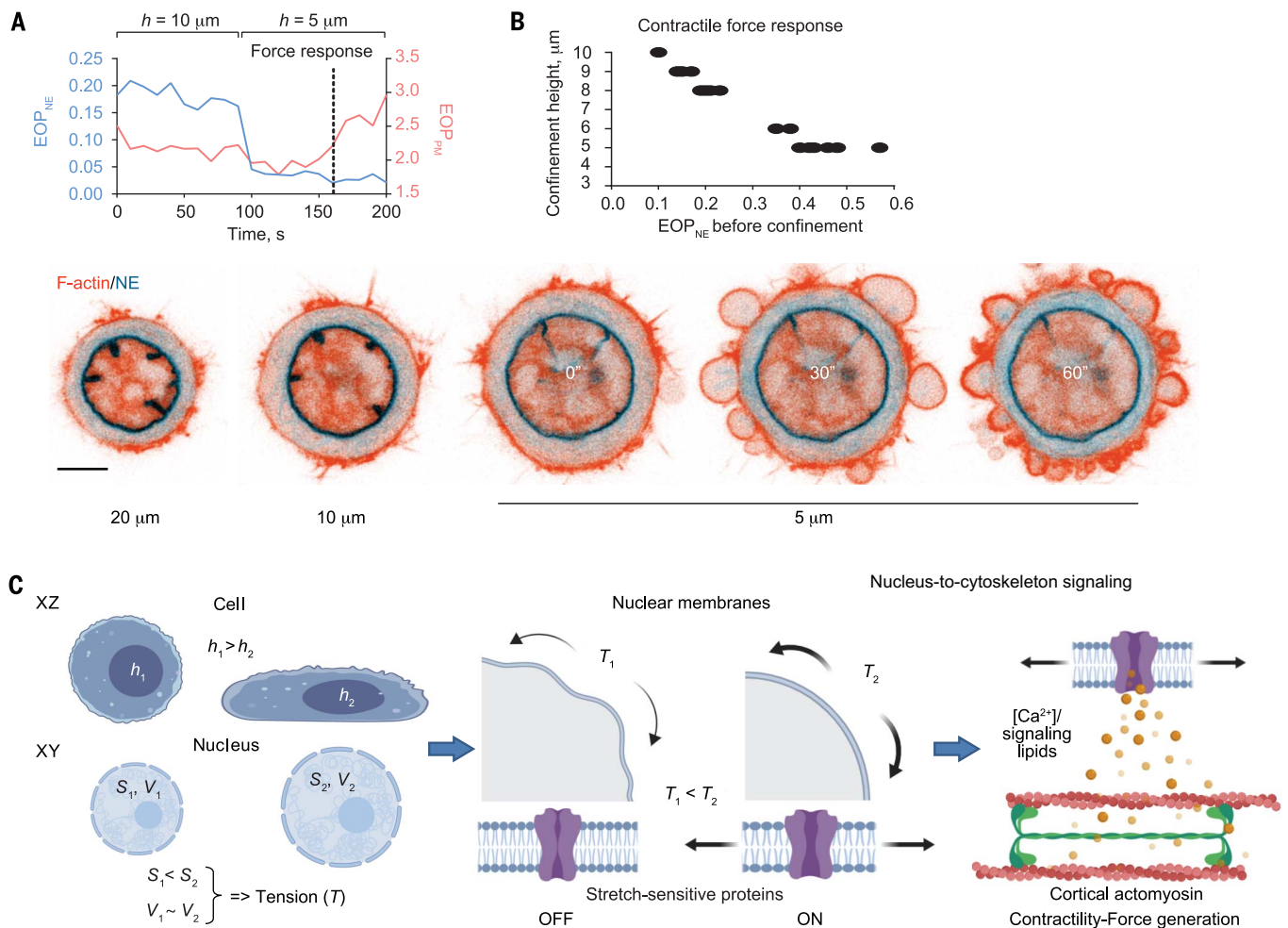
Fig. 3. The nuclear ruler working model. (**A**) (Top) Representative graph of temporal evolution of NE unfolding (EOP_{NE}, blue) and PM blebbing (EOP_{PM}, red). (Bottom) Time-lapse image sequence of the LAP2-GFP–labeled NE (blue) and Lifeact-mCherry–labeled F-actin (red) in the same live cell responding to the sequential confinement to 20, 10, and 5 μm. Scale bar, 5 μm. (**B**) Height for the onset of contractile force response as a function of the degree of NE folding (EOP_{NE}) before confinement (*n* = 20 cells).

(**C**) Sketch of the working model: Cells use the nucleus as an internal ruler for their height. When a cell deforms below the resting height (h_1) of its nucleus, the nuclear surface area (S) increases while the nuclear volume (V) remains constant. At a critical height (h_2), the NE fully expands and gets stretched increasing its tension (T). The increase in NE tension stimulates stretch-sensitive proteins whose activity promotes and/or reinforces cortical actomyosin contractility.

kinase MLCK, and the NE tension sensor cPLA2 were required for the contractile response, pointing to a signal emanating from the perinuclear ER and/or the NE to activate actomyosin contraction at a specific confinement height. Consistently, imaging of intracellular calcium with the GCaMP6 calcium biosensor revealed a strong increase in cytosolic calcium upon 5-μm confinement (fig. S5A), which was inhibited by blocking intracellular stretch-sensitive calcium channels InsP3Rs with 2APB (fig. S5B), but not via chelation of extracellular calcium with BAPTA (fig. S5A). Conversely, adding ionomycin (to artificially increase cytosolic calcium concentration) or the signaling lipid arachidonic acid (ARA) [an omega-6 fatty acid that can be produced in a NE stretch-sensitive manner via enzymatic activity of cPLA2 on nuclear membranes (17)] to cells confined to 10 μm induced persistent blebbing without further confinement (fig. S5C). Finally, analysis of the supernatant of a population of confined cells (using a microfabricated confinement device; see materials and methods) showed an increase in ARA production upon 5-μm confinement, which is lost upon cPLA2 inhibition with AACOCF3/AA (fig. S5D). Notably, unlike Y27632, which globally perturbed basal cell contractility at both 10 and 5 μm, the drugs yielding a phenotype in our mini-screen exerted their effect only at 5 μm, as follows from our measurements of cortical cell tension, cell pressure, and myosin cortex-to-cytosol ratio at 10 μm (fig. S5E). This indicated that the targets of the drugs become functionally engaged in a trigger-like fashion when the cell is confined below 10 μm. These results, together with the controls for drugs activity (fig. S5F), suggested that the nuclear membrane compartment, continuous with the perinuclear ER, might be involved in measuring the cell dimensions and triggering the contractile response below a specific confinement height.

The trigger height for contractile cell responses is determined by NE tension

To understand how the NE–perinuclear ER and associated signaling pathways could be engaged in triggering the sustained contractile response of cells to a specific confinement height, we decided to characterize nuclear shape and deformation state at 20-, 10-, and 5-μm confinement (Fig. 2B). We observed that the nuclear volume undergoes only very minor changes, whereas projected surface area of the nucleus increases substantially between 10- and 5-μm confinement (Fig. 2C), suggesting a potential expansion of the NE. Indeed, we found that the NE in rounded nonadherent cells displays large folds and wrinkles, which become less prominent at 10 μm and completely disappear at 5 μm (Fig. 2D). To characterize this phenomenon quantitatively, we estimated the NE folding index by measuring

the excess of the perimeter of the NE (EOP_{NE}) in the same single cell at various heights or by statistically comparing this parameter across populations of cells confined to a specific height. We found that EOP_{NE} decreases as cells get more confined [Fig. 2D; we also confirmed this result with an additional metric: standard deviation of the local curvature along the NE perimeter (fig. S5G)]. Unconfining cells led to a rapid refolding of the envelope, concomitant with the loss of the contractile response (Fig. 2E). These measurements suggested that within the range of confinement heights applied in our experiments, the nucleus maintains a constant volume by progressively unfolding its envelope until it reaches a fully unfolded state at 5 μm. A higher degree of confinement and more severe nuclear compression result in a substantial loss of nuclear volume [reported previously on the basis of micropipette aspiration experiments (19)] and, eventually, NE

rupture events that become predominant below 3-μm confinement height (20).

As the NE fully unfolds, it is likely to reach a state in which it stretches and becomes tensed. To estimate this parameter, we first measured the thermally and actively driven fluctuations of the NE on the time scale of seconds [see materials and methods and (21)]. We found that the amplitude of the fluctuations systematically decreases as cells get more confined (Fig. 2F), consistent with an increase in the NE tension. Imaging nuclear pores in the NE of the same cell at various heights showed that confinement from 10 to 5 μm causes neighboring nuclear pores to become more distant from each other, consistent with a stretching of the NE (Fig. 2G). Finally, we observed that the mKate2-tagged phospholipase cPla2, sensing lipid crowding in the NE (17), remains in the nucleoplasm at 10 μm but relocalizes to the NE at 5 μm
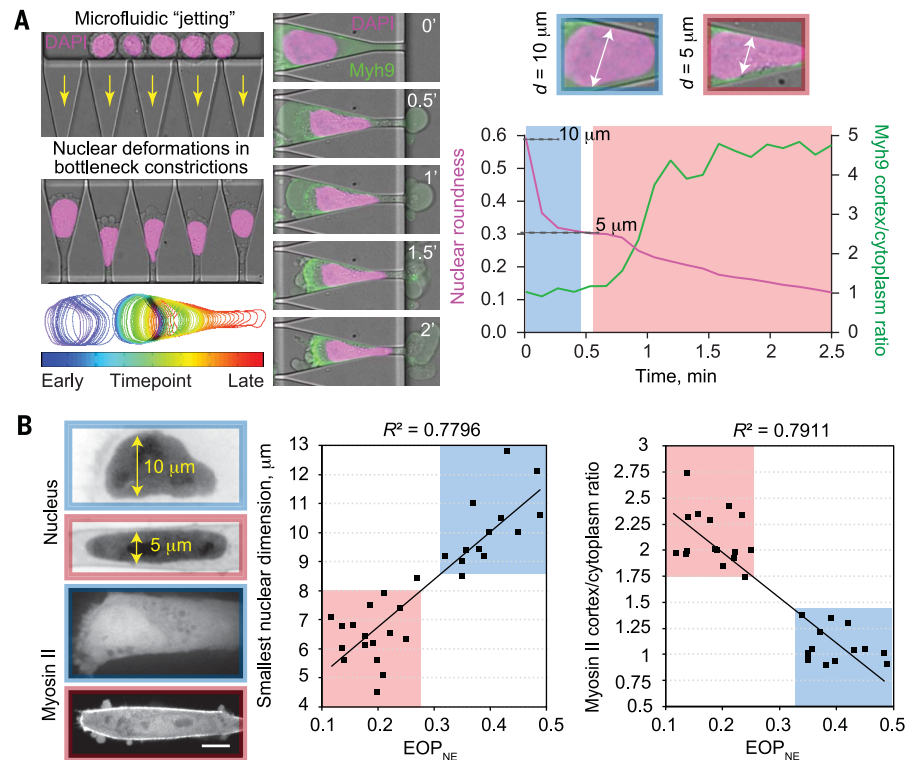
Fig. 4. Correlation between nuclear stretching and cortical recruitment of myosin in experimentally deformed and spontaneously moving cells. (**A**) (Left) Representative images of DAPI-stained (magenta) HeLa-Kyoto cells microfluidically pushed into bottleneck PDMS constrictions. Color-coded nuclear outlines at different time points for a cell pushed into the constriction are shown at the bottom. (Middle) Representative image sequence of the nucleus (magenta) and MYH9-GFP–labeled myosin (green) in a live cell pushed into the constriction. (Right top and bottom) Images of the nucleus inside the bottleneck constriction reaching roundness equivalent to 10- and 5-μm confinement heights, and graph of the nuclear roundness index (magenta) and myosin cortical recruitment (green) in time representative of n = 30 cells. (**B**) (Left) Representative images (xy views, single confocal slices) of RFP-NLS–labeled nuclei (top) and GFP-MLC2–labeled myosin in HT1080 cells within 3D CDM. (Middle) Smallest nuclear dimension plotted against corresponding values of EOP_{NE}. (Right) Myosin cortex-to-cytoplasm ratio plotted against corresponding values of EOP_{NE} (n = 30 cells). Scale bar, 5 μm.

(Fig. 2H), a transition previously shown to be triggered by nuclear membrane tension increase and to correspond with cPLA2 enzyme activation (*17*). Overall, these observations suggested that confinement to 5 μm stretches the NE.

To assess whether the height threshold at which cells display the active contractile response coincides with the induction of NE stretching, we took advantage of the variety of nuclear shapes and folding states in the cell population and systematically investigated these parameters along with contractile force and cell morphology readouts. First, correlative recording of F-actin and the NE (Fig. 3A, bottom images) enabled us to observe that NE unfolding temporally precedes the onset of the contractile response (Fig. 3A, top graph, and movie S3), with a delay of 38 ± 17 s (*n* = 20 cells). This is compatible with a causal link between the NE unfolding-stretching and the onset of a sustained contractile response. Second, we found that cells with more folded nuclei before confinement (larger EOP_{NE}) start to contract at a lower confinement height (Fig. 3B), indicating that the degree of NE folding sets the sensitivity threshold for the ability of cells to discriminate between different confinement heights.

Because we used cultured proliferating cells in our experiments, a source of cell-to-cell variability in responses to confinement could come from the cell cycle stage, which introduces a natural range of NE states in a cell population (*21*). Therefore, we decided to test a FUCCI HeLa cell line expressing fluorescent cell cycle stage markers in our confinement experiments. We determined that unconfined G_1 cells have significantly higher values of EOP_{NE} than G_2 cells (fig. S5H). Whereas the unconfined cell height and mechanical state (basal cortical tension and cell pressure) at 10-μm confinement were similar for rounded, nonadherent G_1 and G_2 cells (fig. S5H), G_2 cells required less confinement than G_1 cells to trigger the contractile response (fig. S5H, bottom right graph). This result further confirmed that the state and size of the nucleus defines a ruler to trigger the active contractile cell response. It also suggested that the nuclear ruler might render proliferating cells more or less sensitive to deformations, depending on their cell cycle stage.

The nuclear ruler working model

Collectively, our results suggested the following working model (Fig. 3C): Each single cell in the rounded state has a certain nuclear volume and an excess of NE surface area stored in NE folds. When one of the dimensions of the cell is reduced below the resting nuclear diameter, the nucleus deforms and its envelope unfolds. Once the NE reaches full unfolding, it stretches, potentially together with the perinuclear ER, leading to calcium release from internal stores and cPLA2 relocalization onto the stretched NE, followed by cPLA2 enzyme activation and production of ARA. Both calcium ions and ARA are classical second messenger molecules with a well-known stimulatory effect on actomyosin contractility (*22–24*), thus mechanistically linking cell height to cell contractility. Consistent with this model, the correlative live recording of cPla2-mKate2, calcium (GCaMP6-EGFP), and forces during cell height change from 10 to 5 μm and show relocalization of cPla2 within 20 s and intracellular calcium increase within less than 1 min, both phenomena preceding the contractile response of the cell (fig. S5I).

A first direct prediction of the nuclear ruler model is that as cells start squeezing through a tissue opening with a size smaller than a resting nuclear diameter, they should deform, unfold, and stretch their nuclei. This activity would lead to an increase in cortical myosin concentration. To test this prediction in a controlled and quantitative manner, we microfluidically flowed HeLa cells through microchannels with bottleneck constrictions. We found that nuclear deformations reflected in changes of the nuclear roundness index precede myosin accumulation at the cortex and that this takes place when the nuclear diameter is changed to ~5 μm, but not 10 μm (Fig. 4A). To examine whether these dependencies can be observed in spontaneously migrating cells in a more physiological context, we looked at invasive HT1080 cells maneuvering through a 3D CDM. By plotting myosin cortical accumulation against the PM excess of perimeter (i.e., cell blebbing and thus contractility measure), we verified that our measure of myosin recruitment at the cell cortex is a good predictor of the degree of cell contractility in 3D (fig. S6). This parameter scaled with the extent of
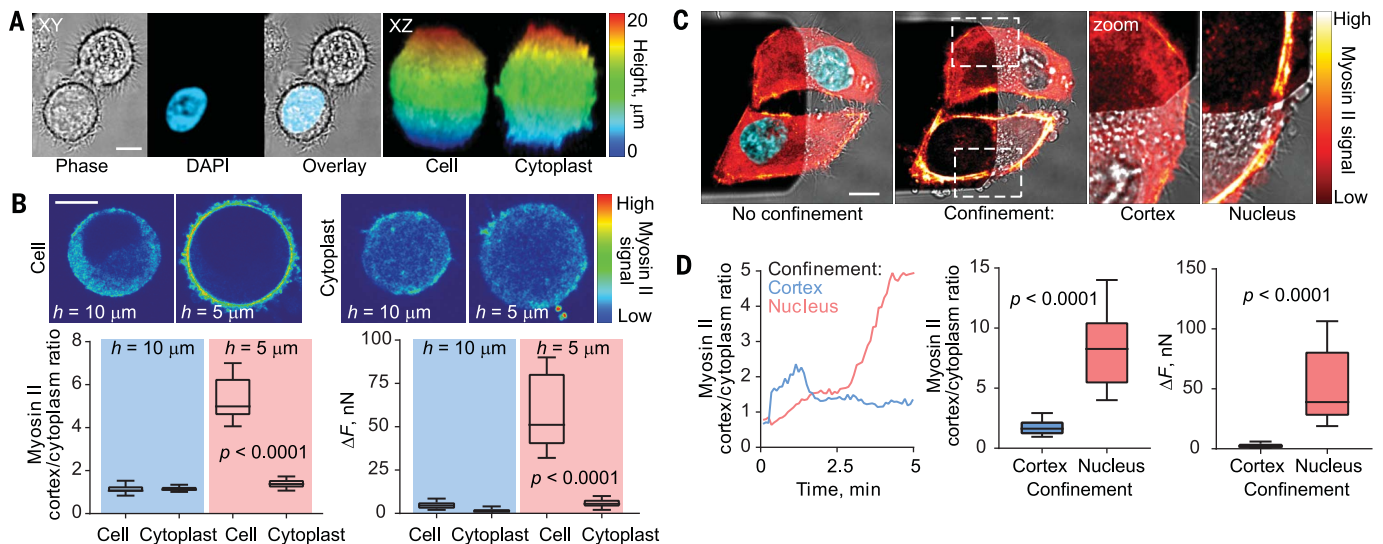
Fig. 5. Enucleated cells and cells regioselectively confined to avoid the nucleus do not trigger contractile responses at relevant heights. (**A**) (Left) Representative images (*xy* views) of a nucleated [DAPI (blue)–positive] cell and an enucleated (DAPI-negative) cytoplast. (Right) *xz* views of a cell and a cytoplast of similar height representative of those selected for analyses. Scale bar, 5 μm. (**B**) Images (top) and quantifications (bottom) of myosin cortical accumulation (left) and force response (Δ*F*, right) in cells (*n* = 10) and cytoplasts (*n* = 10) confined to 10 versus 5 μm. Data are from ≥2 experiments; mean ± SD; *P* value, unpaired *t* test. Scale bar, 10 μm. (**C**) Regioselective confinement of the nuclear region (lower cell) versus the nucleus-free lamella (upper cell). Cyan, DAPI nuclear stain; Red hot, myosin signal; Dashed squares, zoomed regions (right images). Scale bar, 10 μm. (**D**) Quantifications of myosin cortical accumulation and force response (Δ*F*) upon nuclear (*n* = 10) and lamellar cortex (*n* = 10) confinement. Data are from ≥2 experiments; mean ± SD; *P* value, unpaired *t* test.

nuclear surface folding, which in turn was dependent on the smallest nuclear dimension (Fig. 4B). These data showed that both imposed and spontaneous nuclear deformations observed in migrating cells correlate with the contractile response, suggesting that the nuclear ruler could be relevant in physiological contexts such as cells circulating in blood capillaries or migrating through dense tissues.

Cells without the nucleus show defective contractile responses to spatial confinement

A second prediction of our working model is that removing the cell nucleus should affect the contractile response to confinement. We thus produced cytoplasts by cell enucleation using centrifugation (25). This resulted in a mixed population of enucleated cytoplasts and nucleated cells (Fig. 5A). Cytoplasts, on average, had a smaller volume than nucleated cells (fig. S7A) but a rather similar height (cell volume scales to the cubic root of cell diameter). Thus, we were able to compare nucleated cells and enucleated cytoplasts of similar initial heights confined to 10 and 5 μm. Whereas nucleated cells showed the expected contractile response at 5 μm, this was not the case for enucleated cytoplasts (Fig. 5B and movie S4). Cytoplasts were not deficient in the contractile response pathway, because confining them further to 1 μm triggered both a force response and myosin recruitment at the cortex (fig. S7B), although to a significantly lesser extent than nucleated cells at 5 μm. Moreover, although the response of cytoplasts was reduced upon treatment with 2APB inhibiting

calcium release from internal stores, it was not affected by treatment with the cPLA2 inhibitor AACOCF3 (fig. S7B). This suggested that the pathway triggered at 1 μm in cytoplasts could be different from that activated in nucleated cells at 5 μm. Such pathway might involve direct compression of other endomembranes [e.g., the ER that remained present in enucleated cytoplasts (fig. S7C)].

To further demonstrate the difference in responsiveness to confinement provided by the nucleus versus the rest of the cell, we used spread nucleated cells and took advantage of the small size of the wedged cantilever tip to apply a local deformation on the cell (Fig. 5C). This experiment showed that locally compressing the cell cortex in the lamellar region, even down to <1 μm (fig. S8 and movie S5), produces only a very transient response, whereas confining the part of the cell that contains the nucleus results in a sustained contractile response (Fig. 5D and movie S6). Upon nuclear deformation, myosin cortical recruitment occurred even in the region that was not directly confined (Fig. 5D). This showed that the contractile response is not due to the cell deformation per se, but rather to a signal that could get released locally and propagate away from the nucleus (indeed, the increase in contractility in the nonconfined part manifested with a slight delay compared with that in the nuclear region; movie S6). In conclusion, consistent with our working model, the nucleus is required to set the size at which the contractile response is triggered, and the

deformation of nuclear or nucleus-associated compartments is necessary to trigger the sustained response.

Cells with altered NE properties have a defective nuclear ruler

We further tested the nuclear ruler model by affecting the stiffness and the folded state of the NE. Lamin A/C–depleted cells (fig. S9A) displayed nuclear dysmorphia and a floppier (Fig. 6A) but did not undergo excessive cell death, even upon confinement to 5-μm height (fig. S9B), at which the depleted cells also show a high rate of NE ruptures (Fig. 6A, bottom left graph). This mechanical instability of the NE, together with the modifications of NE viscoelastic properties upon lamin A/C depletion, could contribute to the relaxation of tension in the envelope. Although volume, projected area (fig. S9C), and surface folding (fig. S9D) of lamin A/C–depleted nuclei were not significantly affected, we found that NE fluctuations in the depleted cells did not decrease in response to 20-, 10-, and 5-μm confinement (Fig. 6A, top right graph), in contrast to control cells (Fig. 2F). This suggested that the envelope of depleted nuclei remained floppy at all confinement heights. Confinement of depleted cells to 5 μm did not trigger intracellular calcium release, nor did it increase levels of ARA production (fig. S9E, "5 μm confinement" subpanel). Consistently, although their basal mechanics were unaltered at 10 μm (fig. S9E, "10 μm confinement" subpanel), the depleted cells displayed an attenuated contractile response at 5-μm confinement (Fig. 6A, bottom right graph, and fig. S9F). This finding is consistent with the nuclear ruler model and further suggests that the level of lamin A/C, which varies considerably in different cell types and environmental conditions, can modulate the response of cells to spatial confinement by affecting the mechanical properties of the NE.

The inner nuclear membrane and ER membrane protein lamin B receptor (LBR) is known to control NE folding in a dose-dependent manner (26). Its overexpression leads to perinuclear ER expansion and overproduction of NE membranes, which in turn provides additional NE surface area to accommodate excess membrane protein (27, 28). Indeed, our measurements of nuclear surface folding showed that LBR-GFP overexpressing (OE) cells have a highly folded nucleus and fail to unfold it in response to 5-μm confinement, in contrast to LAP2/LAP2b-expressing (control) cells (Fig. 6B, images and top graph, and fig. S9G). Consistently, LBR overexpression abrogated both cytoplasmic calcium increase and levels of ARA production at 5 μm (fig. S9H, "5 μm confinement" subpanel). Although their basal cortical mechanics were unaltered at 10 μm (fig. S9H, "10 μm confinement" subpanel), LBR-GFP OE cells significantly impaired contractile responses
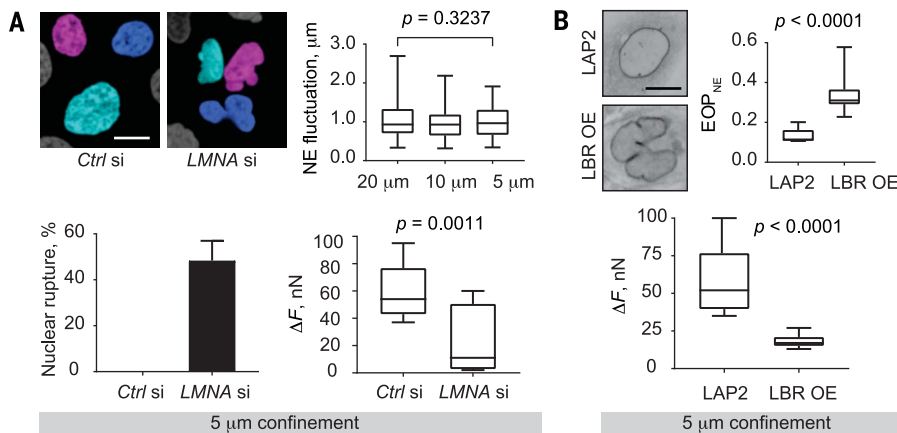
Fig. 6. The nuclear ruler is defective in cells with altered NE properties. (**A**) (Top left) Representative images of DAPI-stained nuclei in HeLa-Kyoto cells treated with control or *LMNA* siRNA. (Top right) Quantifications of NE fluctuations in *LMNA* siRNA-treated cells under 20-, 10-, and 5-μm confinement (data are from ≥2 experiments; mean ± SD; *n* = 20 cells per height; *P* value, unpaired *t* test). (Bottom left) Percentage of cells displaying nuclear rupture at 5 μm. Data are from ≥2 experiments; *n* = 15 cells per condition. (Bottom right) Force response (Δ*F*) to 5-μm confinement. Data are from ≥2 experiments; mean ± SD; *n* = 10 (*Ctrl* si) and 15 (*LMNA* si) cells; *P* value, unpaired *t* test. Scale bar, 10 μm. (**B**) (Top) Representative images of NE in HeLa-Kyoto cells stably expressing LAP2-GFP or ectopically overexpressing (OE) LBR-GFP and corresponding EOP$_{NE}$ quantifications. Data are from ≥2 experiments; mean ± SD; *n* = 10 cells per condition; *P* value, unpaired *t* test. (Bottom) Force response (Δ*F*) to 5-μm confinement. Data are from ≥2 experiments; mean ± SD; *n* = 10 (LAP2) and 15 (LBR OE) cells; *P* value, unpaired *t* test. Scale bar, 10 μm.

Fig. 7. The nuclear ruler function in immune cell migration. (**A**) (Left and middle) Cartoons illustrating primary culture of iDCs and their confinement between two parallel surfaces inducing a highly migratory DC phenotype. (Right top) iDC velocity measured at 10-μm (n = 20 cells), 4-μm (n = 35 cells), and 3-μm (n = 35 cells) confinement height (h). (Right bottom) Cell velocity (v_{cell}) measured at 3-μm confinement in control [DMSO and wild-type (WT)] versus cPLA2-inhibited (AACOCF3/AA treatment) or *Lmna* knockout (KO) cells (n = 20 cells per condition). Data are from ≥2 experiments; mean ± SD; P value, unpaired t test. (**B**) (Top) Temporal color-coded cell tracks from a representative time-lapse movie of control (*Ctrl si*) and cPLA2a-depleted (*Pla2g4a si*) LifeAct-GFP–expressing iDCs under 3-μm confinement. (Bottom) Statistical analysis of cell velocity (v_{cell}) for control and depleted cells at 4- versus 3-μm confinement. Data are from ≥2 experiments; mean ± SD; n = 20 cells per condition; P value, unpaired t test. Scale bar, 50 μm. (**C**) Representative images of DAPI-stained nuclei (xy view, single confocal slices) and EOP_{NE} quantifications in iDCs at 4- versus 3-μm confinement. Data are from ≥2 experiments; mean ± SD; n = 35 cells per condition; P value, unpaired t test. Scale bar, 5 μm. (**D**) Representative images and quantifications of myosin cortical accumulation in control (*Ctrl si*) and cPLA2a-depleted (*Pla2g4a si*) MYH9-GFP–expressing iDCs at 4- and 3-μm confinement. Data are from ≥2 experiments; mean ± SD; n = 20 cells per condition; P value, unpaired t test. Scale bar, 15 μm.
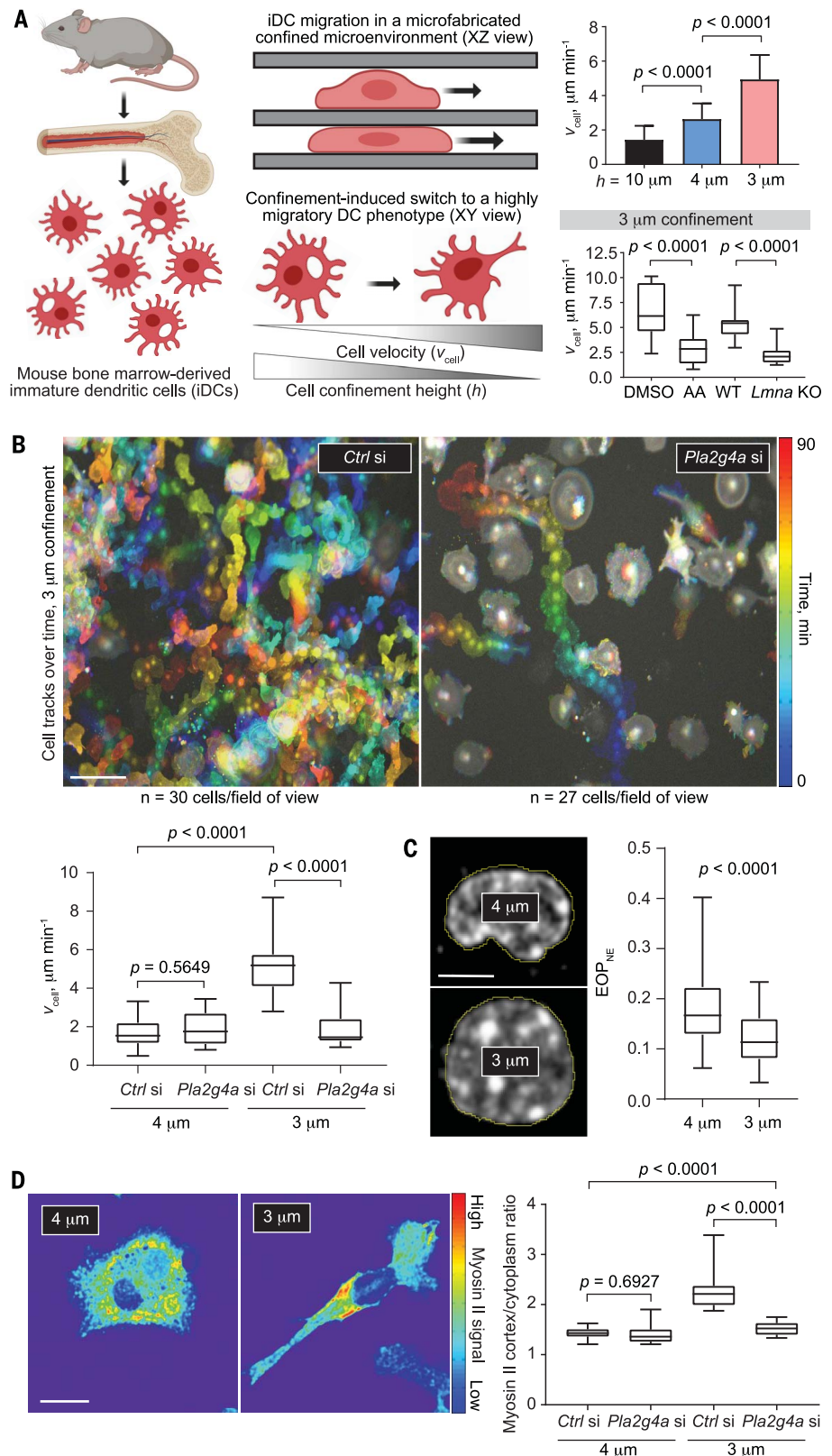
to 5-μm confinement (Fig. 6B, bottom graph, and fig. S9I). Therefore, we concluded that NE folding and unfolding constitutes a key element of the nuclear ruler mechanism. These findings further suggested that modulation of NE com-ponents that affect the extent of NE folding [e.g., LBR and SUN2 (29)] could allow different cell types to trigger responses to various levels of confinement or to measure different ranges of sizes, depending on their function.

The nuclear ruler participates in adaptive modulation of cell propulsion during confined migration

We hypothesized that the nuclear ruler mech-anism can be used by migrating cells to increase
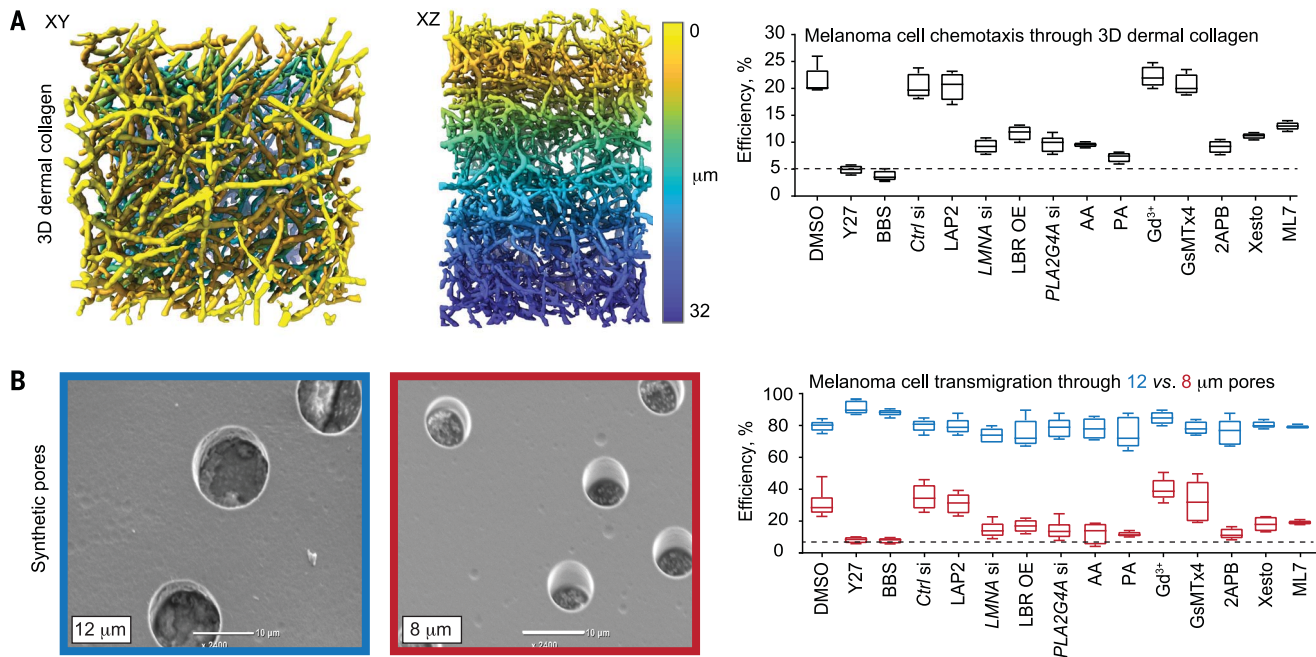
Fig. 8. The nuclear ruler function in cancer cell migration. (A) (Left) 3D light-sheet microscopy images of atelopeptide fibrillar bovine dermal collagen (1.7 mg ml^{-1}) lattices. (Right) Quantifications of the percentage of human MCs A375P able to chemotactically transmigrate through the lattice (1 mm thick) in the presence of the broad-spectrum matrix metalloproteinase inhibitor GM6001 in conditions affecting cell contractility (Y27, BBS, and ML7), NE properties (LMNA si and LBR OE), cPLA2 expression and activity (PLA2G4A si, AA, and PA), and stretch-sensitive calcium release (Gd^{3+}, GsMTx4, 2APB, and Xesto). Data are from ≥2 experiments; mean ± SD; n ≥ 300 cells per condition. See table S3 for drug target description and pairwise statistical comparisons; see materials and methods for drug concentrations. (B) Scanning electron microscopy images of polycarbonate membranes with 12-µm (blue) and 8-µm (red) pores (scale bar, 10 µm), and quantifications of the percentage of A375P cells able to chemotactically transmigrate through the pores in the conditions specified in (A). Data are from ≥2 experiments; mean ± SD; n ≥ 300 cells per condition. See table S3 for drug target description and pairwise statistical comparisons; see materials and methods for drug concentrations. The dotted line in (A) and (B) represents the cell transmigration rate upon global perturbation of actomyosin contractility.

their propulsion when surrounding space becomes limited, explaining the switch to fast amoeboid migration upon confinement of slow mesenchymal cells, which we reported previously (8). In support of this hypothesis, we found that single HeLa-Kyoto cells, remaining under the confining AFM cantilever for prolonged periods of time, can spontaneously initiate movement, enabling the cells to evade the cantilever (fig. S10A). We also observed the predicted increase in migration speed upon confinement of immature mouse bone marrow–derived dendritic cell (iDC) populations using our microfabricated confiner device (Fig. 7A) (30). This speed increase was lost upon functional ablation of cPLA2 (Fig. 7A, bottom graph; fig. S10B, upper right graph; and Fig. 7B, right graph) or lamin A (Fig. 7A, bottom graph) (31) and corresponded specifically to the confinement height (3 µm) at which iDC nuclei get fully unfolded (Fig. 7C). Consistently, myosin accumulated at the iDC cortex in a cPLA2-dependent manner specifically at 3 µm (Fig. 7D). A large fraction of iDCs at 3 µm switched to a migratory polarized cell shape phenotype, characteristic of fast-moving cells, that was almost entirely lost upon cPLA2 depletion (Fig. 7B, fig. S10B, and movie S7). Overall, the data obtained from both HeLa-Kyoto

cells and primary iDCs suggested that the nuclear ruler pathway could be involved in triggering a contractile "evasion reflex," helping invasive cells to either rapidly escape or penetrate the most confined regions of dense tissues.

To further test the function of the nuclear ruler in invasive cell migration, we assessed the protease-independent ability of human metastatic skin melanoma cells (MCs), a well-established cellular model employing contractility-driven, amoeboid invasive motion in vivo (32), to chemotactically transmigrate (fig. S10C) through 3D dermal collagen gels or synthetic polycarbonate membranes with different porosity. 3D collagen lattices (Fig. 8A, left images) displayed pore sizes ranging from 1 to 12 µm (fig. S10D), thus representing a heterogeneous, mechanically restrictive environment in which cells are expected to deform their nuclei. Indeed, perturbations targeting the nuclear ruler pathway affected the efficiency of MC transmigration through 3D collagen (Fig. 8A, right graph, and table S3). Consistent with the diameter of their nuclei (11 ± 2 µm, n = 100 cells), MCs were dependent on basal actomyosin contractility or pathways associated with the nuclear ruler only when transmigrating through 8- but not 12-µm pores of polycarbonate membranes (Fig. 8B, left images; fig. S10E; and table S3). These results suggested

that, owing to the nuclear ruler, migratory cells can use the energetically costly actomyosin contractility motor on demand, when the local cell environment becomes restrictive to migration.

Discussion

Collectively, our data establish a nongenetic function for the nucleus as an internal ruler. Relying on this ruler, cells can measure the degree of their environmental confinement and rapidly tailor specific behaviors to adapt to the confinement at time scales shorter than those associated with changes in gene expression. In the context of cell migration, such tailored cellular behaviors might help cells avoid environmental entrapment, which is relevant to cancer cell invasion, immune cell patrolling of peripheral tissues, and progenitor cell motility within a highly crowded cell mass of a developing embryo (33). The nuclear ruler mechanism defines an active function for the nucleus in cell migration, potentially explaining why enucleated cells show a poor motile capacity in dense collagen gels (34). Engaging the nuclear ruler and generating propulsive forces, cells can push their large nucleus through small openings, thus overcoming the rate-limiting effect of the bulky and stiff nucleus on confined migration. However, some highly specialized

and short-lived cells, such as neutrophils, trade nuclear size and stiffness for uncompromised migration through dense tissue regions. To achieve this, maturing neutrophils transcriptionally up-regulate LBR and down-regulate LMNA expression that makes the nucleus highly pliable (35) and might cancel its rate-limiting effect and ruler function in the context of confined migration.

The nuclear ruler mechanism relies on NE tension sensing by the phospholipid-hydrolyzing enzyme cPLA2 (13, 17). The enzymatic activity of cPLA2 is fundamental to the eicosanoid biosynthetic pathway known for its function as an essential mediator of paracrine inflammatory signaling in the immune system, with effects on immune cell contractility and migration (36, 37). The function we propose here relies on direct mechanical activation of cPLA2 and subsequent release of ARA, but it does not exclude the induction of the downstream signaling associated with ARA metabolism. When we confined the nucleus in only one cell of a pair of closely juxtaposed cells, we did not observe any signs of contractility activation in the neighboring cell (fig. S11), which suggests that paracrine signaling might not be sufficient to activate contractility in this case. Fully characterizing the signaling cascade triggered by mechanical activation of the cPLA2 pathway and subsequent changes in lipid metabolism in the context of confined cell migration is an important perspective for future studies. We also showed that the nuclear ruler pathway depends on stretch-activated intracellular calcium release. Here, we pinpointed a role for InsP3Rs, but there are many other stretch-sensitive calcium channels on the ER and nuclear membranes (38) that could contribute to the pathway in a cell type– or context-specific fashion.

Establishing the nucleus as an internal ruler of the extracellular environment opens avenues of research in the field of single-cell migration as well as in tissue homeostasis and developmental biology. Indeed, morphological changes associated with cell spreading on the ECM are known to affect nuclear morphology and cell cycle progression (39). Therefore, the nuclear ruler might contribute to cell fate choices during tissue growth. Given that cell crowding in tissues such as epithelia alters the cell shape and aspect ratio, tissue cells [in addition to the known mechanisms (1)] may use the nucleus as a sensor of local cell density.

Materials and methods
Cell culture

Human cervical adenocarcinoma cells HeLa-Kyoto stably expressing myosin IIA (MYH9)–GFP and LifeAct-mCherry or MYH9-GFP and the PM-targeting CAAX box fused to mCherry, or LAP2/LAP2b-GFP, NUP107-GFP, HeLa (CCL-2) cells stably expressing cPla2-mKate2, human fibrosarcoma cells HT1080 expressing GFP-

myosin light chain 2 and RFP-NLS, primary human foreskin fibroblasts (HFFs), human MCs A375P, N-rasV12 oncogene-transformed rat liver epithelial cells IAR-2, and canine kidney epithelial cells MDCK-2 were maintained in DMEM/F12 supplemented with 10% FBS (Invitrogen) at 37°C and 5% CO_2. Human epidermal stem cells were cultured as previously described (40). All cell lines were tested for mycoplasma contamination using MycoScope PCR Mycoplasma Detection Kit (Genlantis). Mouse bone-marrow–derived immature dendritic cells (iDCs) were obtained by culturing bone marrow cells (from both male and female 8- to 10- week-old LifeAct-GFP mice (41), MYH9-GFP mice (42), and control (JAX mice stock number: 000664) or Lmna KO mice (31) for 10 to 11 days in complete DC medium (IMDM medium supplemented with fetal calf serum (FCS, 10%), glutamine (20 mM), penicillin-streptomycin (100 U/ml), β-mercaptoethanol (50 μM), and granulocyte-macrophage colony-stimulating factor/GM-CSF (50 ng/ml)–containing supernatant obtained from transfected J558 cells.

Transfection procedure, expression vectors, and siRNA oligonucleotides

Cells were transfected with plasmid DNA using Lipofectamine LTX reagent (Invitrogen) transiently or stably, according to manufacturer's protocol. For RNA interference experiments, cells were transfected with small interfering RNA (siRNA) oligonucleotides using Lipofectamine RNAiMAX reagent (Invitrogen), according to manufacturer's protocol. In experiments on cPLA2a knockdown in bone marrow–derived mouse immature dendritic cells (iDCs), the cells were transfected using the Amaxa mouse Dendritic Cell Nucleofector Kit (Lonza).

The following expression vectors were used for plasmid DNA transfections: empty vector pEGFP-C1 (Clontech); Addgene plasmids: 61996 LBR pEGFP-N2 (646) (43), 40753 pGP-CMV-GCaMP6s (44), 86849 pBOB-EF1-FastFUCCI-Puro (45). To knock down LMNA or cPLA2a, cells were transfected with nontargeting siRNA (control) or validated ON-TARGETplus SMARTpool siRNA reagents (Dharmacon) targeting human-specific LMNA mRNA (cat. no. L-004978-00-0005), human-specific PLA2G4A mRNA (cat. no. L-009886-00-0005), or mouse-specific Pla2g4a mRNA (cat. no. L-063167-01-0010). Unless stated otherwise, cells were analyzed 72 hours post-transfection using standard Western blot or immunofluorescent analysis protocols. Based on quantitative densitometry of proteins, the knockdown efficiency was estimated as $84.7 \pm 2.5\%$ (3 repeats). Additionally, lentiviral transductions were performed to achieve lamin A knockdown in HeLa cells. Viral particles were produced by transfection of 0.8 million 293FT cells with 3 μg DNA and 8 μl TransIT-293 (Mirus Bio) per well. For shRNA mediated knockdown

of lamin A, 0.4 μg CMV-VSVG, 1 μg psPAX2 and 1.6 μg of either pLKO.1-puro-LMNAsh4 (TRCN0000061837, target sequence GCCGTG-CTTCCTCTCACTCAT) or pLKO1puro-shLACZ (target sequence GCGATCGTAATCACCC-GAGTG) as negative control were combined. Viral supernatants were harvested 48 hours post-transfection, filtered at 0.45 μM, and added on to HeLa cells that had been seeded 1 day before transduction at a 2:1 ratio of viral supernatant:medium containing protamine at a final concentration of 1 μg/ml. Cells were washed once in PBS and passaged at 48 hours post-transduction with 2 μg/ml of puromycin for selection of stably transduced cells.

Drug treatments

The following pharmacological inhibitors and chemical compounds were used: 10 μM ROCK-mediated contractility inhibitor Y27632 (Y27) (EMD), 10 μM myosin II ATPase inhibitor blebbistatin (BBS) (Toronto Research Chemicals), 20 μM Ca^{2+}-sensitive myosin light chain kinase/MLCK inhibitor ML-7 (Sigma-Aldrich), 1 mM apoptosis inducer hydrogen peroxide (H_2O_2), 1 μM transcription inhibitor triptolide (TRP) (Tocris Bioscience), 50 μg ml^{-1} translation inhibitor cycloheximide (CHX) (Sigma-Aldrich), 1 μM AZD6738 inhibiting the Serine/Threonine protein kinase Ataxia Telangiectasia and Rad3 related (ATR) capable of sensing NE tension (Tocris Bioscience), 10 μM nonspecific PM permeability marker propidium iodide (PI) (Sigma-Aldrich), 0.4 mM PM tension reducer sodium deoxycholate (DOCL) (Sigma-Aldrich), 10 μM gadolinium (III) chloride (Gd^{3+}) or 5 μM peptide GsMTx4 from the tarantula venom affecting mechanosensitive ion channels on the PM (Tocris Bioscience), 2 mM extracellular Ca^{2+} chelator BAPTA (Sigma-Aldrich), 10 μM intracellular Ca^{2+} chelator BAPTA-AM (Sigma-Aldrich), 10 μM ionomycin (IOM) directly facilitating the transport of Ca^{2+} across the PM (Sigma-Aldrich), 70 μM signaling lipid arachidonic acid (ARA) (a product of enzymatic activity of the NE stretch-sensitive enzyme cPLA2) activating actomyosin contractility (Cayman Chemical), 20 μM AACOCF3 (AA) or 10 μM PACOCF3 (PA) inhibiting the NE stretch-sensitive enzyme cPLA2 (Tocris Bioscience), 100 μM 2APB or 10 μM Xestospongin C (Xesto) blocking stretch-activated inositol triphosphate receptors (InsP3Rs) on the ER/nuclear membranes (Tocris Bioscience), and 20 μM broad-spectrum matrix metalloproteinase inhibitor GM6001 (Merck Millipore). Growth medium was supplemented with 1% DMSO (vol/vol) (Sigma-Aldrich) in control experiments.

Western blotting

Cells were collected and resuspended in Laemmli buffer. Proteins were separated using sodium dodecyl sulfate polyacrylamide gel electrophoresis

(SDS-PAGE) and transferred onto PVDF membranes. After incubation with primary [Lamin A/C antibody no. 2032 (Cell Signaling Technology), cPLA2a antibody no. PA5-29100 (Invitrogen), and GAPDH antibody no. #ab9483 (Abcam)] and secondary [IRDye and VRDye (LI-COR)] antibodies, the membranes were visualized using Odyssey CLx Infrared Imaging System (LI-COR).

Quantitative PCR (qPCR)

To assess the efficacy of the siRNA treatment, qPCR was carried out on iDCs after 48 hours of the siRNA treatment. RNA extraction was performed using RNeasy Micro RNA kit (Qiagen), according to the manufacturer's protocol. cDNA was produced using the high capacity cDNA synthesis kit (Thermo Fisher), according to the manufacturer's protocol, starting from 1 μg of RNA. Quantitative PCR experiments were performed using Taqman Gene Expression Assay (Applied Biosystems) and carried out on a Lightcycler 480 (Roche) using the settings recommended by the manufacturer. The following primers were used: Mm01284324_m1 for PLA2g4 and Mm99999915 for GAPDH as a control. cPLA2a expression was assessed in si-control and si-cPLA2a iDCs. Samples were run in triplicate for each condition. Data were subsequently normalized to GAPDH values, and to the values obtained in control iDCs. The fold change was calculated using the formula $2^{-\Delta\Delta CT}$.

Single-cell flat AFM-based confinement coupled to live cell imaging

Trypsinized cells were resuspended in CO_2-independent, phenol red-free DMEM/F-12 medium supplemented with 10% FBS (Invitrogen) and plated on glass-bottomed 35-mm dishes (FluoroDish, WPI). Experiments with nonadherent cells were initiated 30 min after cell plating to allow for cell sedimentation. Spread cells were obtained 6 hours post cell plating. Dishes with cells were mounted in a dish heater (JPK Instruments) and kept at 37°C under an inverted light microscope (Axio Observer.Z1; Zeiss) equipped with a confocal microscope unit (LSM 700; Zeiss) and AFM head (CellHesion 200; JPK Instruments).

Focused ion beam (FIB)–sculpted, flat silicon microcantilevers were processed and calibrated as described in (46). The microcantilevers were fixed on a standard JPK glass block and mounted in the AFM head. The cantilever was lowered on the cell to a preset height with a constant speed of $0.5 \ \mu m \cdot s^{-1}$, and the resulting varying force and cantilever height were recorded over time. At the same time, differential interference contrast and fluorescence images at the midplane of the confined cell (the imaging settings were readjusted to the medial plane of the cell each time the cell was confined to a specific height) were recorded every 5 s using a 63× water immersion objective. All microscopy equipment was placed, and experiments were carried out in a custom-made isolation box.

Determination of cell pressure and cortical tension

Cell geometry, pressure, and cortical tension were measured on the basis of AFM and imaging data, as described in (46) and (47).

Production of cytoplasts

Enucleated cells were generated as described in (25) and (48).

Microfabrication-based confinement of cell populations

To obtain large quantities of confined cells for cell population or biochemical studies, cell confinement was performed using a homemade device (8) consisting of a suction cup made in polydimethylsiloxane (PDMS, RTV615, GE) used to press a confining coverslip bearing PDMS microspacers (micropillars) on top of the culture substrate populated with cells. The height of the micropillars (10 μm versus 5 μm) determines the height for spatial confinement of cells between the coverslip and the substrate. A version of the cell confiner adapted to multiwell plates was used to perform multiple experiments in parallel (20). The molds for the PDMS microspacers were fabricated following standard photolithography procedures. The surface of the confining side was always treated with nonadhesive pLL-PEG (SuSoS).

Assaying activation of apoptosis in live cells

To detect levels of active apoptotic caspases, the Image-iT LIVE Red Poly Caspases detection kit based on a fluorescent inhibitor of caspases (FLICA) methodology (I35101, Molecular probes) was used according to the manufacturer's protocol.

Biochemical measurements of ARA release

Cells were confined using microfabricated devices as described in the subsection "Microfabrication-based confinement of cell populations." Confinement was released, and the cells were immediately extracted with Dole's solution (heptane, isopropyl alcohol, 1 N sulfuric acid; 10:40:1). Pentafluorobenzyl esters of the fatty acids were prepared and quantified by gas chromatography–mass spectrometry with reference to an internal standard of d8-AA as described in (49).

Epithelial monolayer stretching

A custom-made stretching device was used to perform epithelial monolayer stretching experiments, as described in (1).

Chemotactic transmigration assays

Serum-starved A375P cells were harvested and transferred in serum-free medium to the upper compartment of 5-μm-pore, 8-μm-pore (cat. No. 3421 and 3428, Corning), or 12-μm-pore (cat. no. CBA-107, Cell Biolabs Inc.) polycarbonate membrane inserts (transwells). Cell density was adjusted according to the specific area of each transwell with 5×10^4, 1.5×10^5, and 7.5×10^5 cells added to 5-, 12-, and 8-μm transwells, respectively. Cells were allowed to transmigrate toward the lower compartment containing 10% FBS for 12 hours. Transmigration efficiency was calculated as number of cells at the lower compartment divided by the number of cells added to the upper compartment of a transwell.

To examine the ability of A375P cells to chemotax through 3D collagen gels, atelopeptide fibrillar bovine dermal collagen (cat. no. 5005-B; PureCol, Advanced BioMatrix) was prepared at 1.7 mg ml^{-1} in DMEM and allowed to polymerize in the upper compartment of the 12-μm-pore polycarbonate membrane insert (cat. no. CBA-107, Cell Biolabs Inc.). Serum-starved cells were seeded on top of the collagen pad in serum-free medium, allowed to adhere and transmigrate through the collagen layer and the membrane toward the lower compartment containing 10% FBS for 24 hours. Transmigration efficiency was calculated as number of cells at the lower compartment divided by the number of cells added to the upper compartment of the transwell.

Generation of 3D CDMs

HFFs were plated at high density on gelatin-coated and glutaraldehyde-treated 35-mm (4×10^5 cells, MatTek) or 50-mm (5.7×10^5 cells, Warner Instruments) glass-bottom dishes. Cultures were maintained for 10 days, adding new media with 50 μg/ml ascorbic acid every other day. The matrices were denuded of cells by adding extraction buffer (20 mM NH_4OH and 0.5% Triton X100 in PBS) for 10 min at room temperature and washed with PBS.

Quantitative image analysis

Fluorescence intensity levels (mean gray values, arbitrary units) were obtained from background subtracted images using the ImageJ/Fiji software (NIH; http://rsb.info.nih.gov/ij/index.html).

The Imaris (version 8.3) image analysis software (Bitplane) was used to measure nuclear volume reconstructed from 3D confocal microscopy images.

The dimensionless parameter excess of perimeter (EOP) was calculated to estimate the amount of NE or PM area stored in macro- and microfolds. To calculate EOP, we first obtained values for perimeter (P) and surface area (A) from 2D images taken at the maximum radius of the nucleus (NE marker LAP2-GFP labeling) or cell (PM marker CAAX box-mCherry labeling). Next, we introduced R_0 as the radius of the circle defined by the area A, which allowed us to compute EOP as the ratio between ($P - 2\pi R_0$) and ($2\pi R_0$). EOP values of a

highly folded object tend to be close to 1, whereas EOP of an object with a smooth surface tend to be close to 0. Additional theoretical calculations were performed to account for experimentally observed changes in nuclear aspect ratio (AR); no significant contribution of AR changes to the measured values of EOP was observed.

Nuclear roundness index was obtained using the shape descriptors tool in ImageJ/Fiji.

The MIPAR v.3.2.3. image analysis software (MIPAR Software) and the Kappa plugin for ImageJ/Fiji (https://github.com/brouhardlab/Kappa/tree/master/docs#fit-the-curve-to-the-data) were used to estimate NE surface curvature.

To measure NE fluctuations, nuclei of live cells expressing LAP2-GFP were recorded using a high frame rate acquisition mode (250 msec per frame) for 5 min. The position of each nucleus was corrected for linear and rotational drift using the Stackreg plugin of the ImageJ/Fiji software. Upon drift correction, the edge of the nucleus was registered at a given angle. NE fluctuations were calculated by measuring the standard deviation of the NE from its mean position. To precisely position the NE, linescans across the NE (intensities along a line of 1 pixel in width perpendicular to the NE) were made at different positions along the NE. For each point along the NE and for each time point in the movie, the point of maximum intensity was calculated on the linescan and a parabola was fitted on points before and after the maxima to determine the localization of the NE with a subpixel resolution. For each position along the NE, the mean position was taken as the mean of all time points. The standard deviation of the position of the NE around this mean position was taken as one measure for the fluctuation of the NE. Each point along the NE contributes one measure. Obtained mean NE fluctuation values were expressed in micrometers. The same approach can be applied to measure PM fluctuations. A floppy, and thus less tensed, membrane is expected to fluctuate more, whereas a membrane under tension exhibits no or diminished fluctuations.

The distance between neighboring nuclear pores (NP-NP distance) was estimated for the same living cell expressing a NP maker NUP107-GFP at different degrees of spatial confinement. To this end, a medial confocal slice of the nucleus was obtained to then trace individual NPs along the NE using the Linescan function of the MetaMorph (version 7.7) software (Molecular Devices). Each individual NP was resolved as a local maximum of fluorescence intensity on the Linescan diagram. The distance between nearest local maxima was represented as NP-NP distance.

HeLa (CCL-2) cells stably expressing the NE tension sensor cPla2-mKate2 (*17*) were used to perform measurements of average fluorescence intensity of the mKate2 signal at the NE vs. the nucleoplasm. Note, cPla2-mKate2 cells (*17*) express highly variable levels of the cPla2-mKate2 construct, making the percentage of cells displaying a robust cPla2-mKate2 accumulation at the NE in response to compression varying from experiment to experiment. Therefore, cells expressing intermediate levels of the cPla2-mKate2 construct were FACS-sorted and used for the analysis. Confocal imaging combined with flat tip AFM compression led to bleaching, which was corrected during image analysis. Importantly, only cells that visually showed a clear NE localization of cPLA2 after confinement were quantified and shown in Fig. 2H (representing approx. 20% of the cells). A more reproducible and robust accumulation of cPla2 at the NE in response to compression can be observed in the presence of ionomycin (*33*).

Cell speed was analyzed using the manual tracking plugin of ImageJ/Fiji.

To measure collagen pore sizes, collagen fibers were imaged via axially swept light-sheet microscopy (*50*). The fibers were then detected from the deconvolved images by applying a steerable filter (*51*) followed by non-maximum suppression. We then calculated pore sizes using a custom-written Matlab code implementing the algorithm described in (*2*).

Statistics and reproducibility of experiments

Unless stated otherwise, statistical significance was determined by two-tailed unpaired or paired Student's *t* test after confirming that the data met appropriate assumptions (normality, homogenous variance, and independent sampling). Statistical data are presented as average ± either SEM or SD. Sample size (*n*) and *P* value are specified in the text of the paper or figure legends. Samples in most cases were defined as the number of cells counted or examined within multiple different fields of view on the same dish or slide, and thus represent data from a single sample within a single experiment. When data from a single sample are shown, they are representative of at least three additional samples from independent experiments.

REFERENCES AND NOTES

1. G. T. Eisenhoffer *et al.*, Crowding induces live cell extrusion to maintain homeostatic cell numbers in epithelia. *Nature* **484**, 546–549 (2012). doi: 10.1038/nature10999; pmid: 22504183
2. J. Renkawitz *et al.*, Nuclear positioning facilitates amoeboid migration along the path of least resistance. *Nature* **568**, 546–550 (2019). doi: 10.1038/s41586-019-1087-5; pmid: 30944468
3. B. Trappmann *et al.*, Extracellular-matrix tethering regulates stem-cell fate. *Nat. Mater.* **11**, 642–649 (2012). doi: 10.1038/nmat3339; pmid: 22635042
4. M. D. Vahey, D. A. Fletcher, The biology of boundary conditions: Cellular reconstitution in one, two, and three dimensions. *Curr. Opin. Cell Biol.* **26**, 60–68 (2014). doi: 10.1016/j.ceb.2013.10.001; pmid: 24529247
5. R. Oria *et al.*, Force loading explains spatial sensing of ligands by cells. *Nature* **552**, 219–224 (2017). doi: 10.1038/nature24662; pmid: 29211717
6. M. Théry, A. Jiménez-Dalmaroni, V. Racine, M. Bornens, F. Jülicher, Experimental and theoretical study of mitotic spindle orientation. *Nature* **447**, 493–496 (2007). doi: 10.1038/nature05786; pmid: 17495931
7. J. Z. Kechagia, J. Ivaska, P. Roca-Cusachs, Integrins as biomechanical sensors of the microenvironment. *Nat. Rev. Mol. Cell Biol.* **20**, 457–473 (2019). doi: 10.1038/s41580-019-0134-2; pmid: 31182865
8. Y.-J. Liu *et al.*, Confinement and low adhesion induce fast amoeboid migration of slow mesenchymal cells. *Cell* **160**, 659–672 (2015). doi: 10.1016/j.cell.2015.01.007; pmid: 25679760
9. V. Ruprecht *et al.*, Cortical contractility triggers a stochastic switch to fast amoeboid cell motility. *Cell* **160**, 673–685 (2015). doi: 10.1016/j.cell.2015.01.008; pmid: 25679761
10. M. P. Stewart, Y. Toyoda, A. A. Hyman, D. J. Müller, Tracking mechanics and volume of globular cells with atomic force microscopy using a constant-height clamp. *Nat. Protoc.* **7**, 143–154 (2012). doi: 10.1038/nprot.2011.434; pmid: 22222789
11. F. Kong, A. J. García, A. P. Mould, M. J. Humphries, C. Zhu, Demonstration of catch bonds between an integrin and its ligand. *J. Cell Biol.* **185**, 1275–1284 (2009). doi: 10.1083/jcb.200810002; pmid: 19564406
12. A. G. Clark, O. Wartlick, G. Salbreux, E. K. Paluch, Stresses at the cell surface during animal cell morphogenesis. *Curr. Biol.* **24**, R484–R494 (2014). doi: 10.1016/j.cub.2014.03.059; pmid: 24845681
13. B. Enyedi, P. Niethammer, A Case for the Nuclear Membrane as a Mechanotransducer. *Cell. Mol. Bioeng.* **9**, 247–251 (2016). doi: 10.1007/s12195-016-0430-2; pmid: 27453760
14. A. Elosegui-Artola *et al.*, Force Triggers YAP Nuclear Entry by Regulating Transport across Nuclear Pores. *Cell* **171**, 1397–1410.e14 (2017). doi: 10.1016/j.cell.2017.10.008; pmid: 29107331
15. A. Kumar *et al.*, ATR mediates a checkpoint at the nuclear envelope in response to mechanical stress. *Cell* **158**, 633–646 (2014). doi: 10.1016/j.cell.2014.05.046; pmid: 25083873
16. N. Itano, S. Okamoto, D. Zhang, S. A. Lipton, E. Ruoslahti, Cell spreading controls endoplasmic and nuclear calcium: A physical gene regulation pathway from the cell surface to the nucleus. *Proc. Natl. Acad. Sci. U.S.A.* **100**, 5181–5186 (2003). doi: 10.1073/pnas.0531397100; pmid: 12702768
17. B. Enyedi, M. Jelcic, P. Niethammer, The Cell Nucleus Serves as a Mechanotransducer of Tissue Damage-Induced Inflammation. *Cell* **165**, 1160–1170 (2016). doi: 10.1016/j.cell.2016.04.016; pmid: 27203112
18. M. Raab *et al.*, ESCRT III repairs nuclear envelope ruptures during cell migration to limit DNA damage and cell death. *Science* **352**, 359–362 (2016). doi: 10.1126/science.aad7611; pmid: 27013426
19. A. C. Rowat, J. Lammerding, J. H. Ipsen, Mechanical properties of the cell nucleus and the effect of emerin deficiency. *Biophys. J.* **91**, 4649–4664 (2006). doi: 10.1529/biophysj.106.086454; pmid: 16997877
20. M. Le Berre, J. Aubertin, M. Piel, Fine control of nuclear confinement identifies a threshold deformation leading to lamina rupture and induction of specific genes. *Integr. Biol.* **4**, 1406–1414 (2012). doi: 10.1039/c2ib20056b; pmid: 23038068
21. F.-Y. Chu, S. C. Haley, A. Zidovska, On the origin of shape fluctuations of the cell nucleus. *Proc. Natl. Acad. Sci. U.S.A.* **114**, 10338–10343 (2017). doi: 10.1073/pnas.1702226114; pmid: 28900009
22. F.-C. Tsai, T. Meyer, Ca2+ pulses control local cycles of lamellipodia retraction and adhesion along the front of migrating cells. *Curr. Biol.* **22**, 837–842 (2012). doi: 10.1016/j.cub.2012.03.037; pmid: 22521790
23. P. Solanes *et al.*, Space exploration by dendritic cells requires maintenance of myosin II activity by IP3 receptor 1. *EMBO J.* **34**, 798–810 (2015). doi: 10.15252/embj.201489056; pmid: 25637353
24. M. C. Gong *et al.*, Arachidonic acid inhibits myosin light chain phosphatase and sensitizes smooth muscle to calcium. *J. Biol. Chem.* **267**, 21492–21498 (1992). pmid: 1328235
25. V. Rodionov, E. Nadezhdina, J. Peloquin, G. Borisy, Digital fluorescence microscopy of cell cytoplasts with and without the centrosome. *Methods Cell Biol.* **67**, 43–51 (2001). doi: 10.1016/S0091-679X(01)67004-3; pmid: 11550480
26. S. Gravemann *et al.*, Dosage effect of zero to three functional LBR-genes in vivo and in vitro. *Nucleus* **1**, 179–189 (2010). doi: 10.4161/nucl.11113; pmid: 21326950
27. Y. Ma *et al.*, Lamin B receptor plays a role in stimulating nuclear envelope production and targeting membrane vesicles to chromatin during nuclear envelope assembly through direct

interaction with importin beta. *J. Cell Sci.* **120**, 520–530 (2007). doi: 10.1242/jcs.03355; pmid: 17251381

28. J. Ellenberg *et al.*, Nuclear membrane dynamics and reassembly in living cells: Targeting of an inner nuclear membrane protein in interphase and mitosis. *J. Cell Biol.* **138**, 1193–1206 (1997). doi: 10.1083/jcb.138.6.1193; pmid: 9298976

29. D. A. Donahue *et al.*, SUN2 Overexpression Deforms Nuclear Shape and Inhibits HIV. *J. Virol.* **90**, 4199–4214 (2016). doi: 10.1128/JVI.03202-15; pmid: 26865710

30. M. Le Berre, E. Zlotek-Zlotkiewicz, D. Bonazzi, F. Lautenschlaeger, M. Piel, in *Methods in Cell Biology* (Elsevier, 2014), pp. 213–229.

31. Y. Kim, Y. Zheng, Generation and characterization of a conditional deletion allele for Lmna in mice. *Biochem. Biophys. Res. Commun.* **440**, 8–13 (2013). doi: 10.1016/j.bbrc.2013.08.082; pmid: 23998933

32. V. Sanz-Moreno *et al.*, Rac activation and inactivation control plasticity of tumor cell movement. *Cell* **135**, 510–523 (2008). doi: 10.1016/j.cell.2008.09.043; pmid: 18984162

33. V. Venturini, F. Pezzano, F. C. Castro, H.-M. Häkkinen, S. Jiménez-Delgado, M. Colomer-Rosell, M. M. Sánchez, Q. Tolosa-Ramon, S. Paz-López, M. A. Valverde, P. Loza-Alvarez, M. Krieg, S. Wieser, V. Ruprecht, The nucleus measures shape deformation for cellular proprioception and regulates adaptive morphodynamics. bioRxiv 865949 [Preprint]. 5 December 2019. https://doi.org/10.1101/865949.

34. D. M. Graham *et al.*, Enucleated cells reveal differential roles of the nucleus in cell migration, polarity, and mechanotransduction. *J. Cell Biol.* **217**, 895–914 (2018). doi: 10.1083/jcb.201706097; pmid: 29351995

35. H. R. Manley, M. C. Keightley, G. J. Lieschke, The Neutrophil Nucleus: An Important Influence on Neutrophil Migration and Function. *Front. Immunol.* **9**, 2867 (2018). doi: 10.3389/fimmu.2018.02867; pmid: 30564248

36. P. V. Afonso *et al.*, LTB4 is a signal-relay molecule during neutrophil chemotaxis. *Dev. Cell* **22**, 1079–1091 (2012). doi: 10.1016/j.devcel.2012.02.003; pmid: 22542839

37. R. Majumdar, A. Tavakoli Tameh, C. A. Parent, Exosomes Mediate LTB4 Release during Neutrophil Chemotaxis. *PLOS Biol.* **14**, e1002336 (2016). doi: 10.1371/journal.pbio.1002336; pmid: 26741884

38. M. T. Alonso, J. García-Sancho, Nuclear Ca(2+) signalling. *Cell Calcium* **49**, 280–289 (2011). doi: 10.1016/j.ceca.2010.11.004; pmid: 21146212

39. J. Aureille *et al.*, Nuclear envelope deformation controls cell cycle progression in response to mechanical force. *EMBO Rep.* **20**, e48084 (2019). doi: 10.15252/embr.201948084; pmid: 31368207

40. F. Watt, B. Simon, D. Prowse, in *Cell Biology* (Elsevier, 2006), pp. 133–138.

41. J. Riedl *et al.*, Lifeact mice for studying F-actin dynamics. *Nat. Methods* **7**, 168–169 (2010). doi: 10.1038/nmeth0310-168; pmid: 20195247

42. Y. Zhang *et al.*, Mouse models of MYH9-related disease: Mutations in nonmuscle myosin II-A. *Blood* **119**, 238–250 (2012). doi: 10.1182/blood-2011-06-358853; pmid: 21908426

43. N. Zuleger *et al.*, System analysis shows distinct mechanisms and common principles of nuclear envelope protein dynamics. *J. Cell Biol.* **193**, 109–123 (2011). doi: 10.1083/jcb.201009068; pmid: 21444689

44. T.-W. Chen *et al.*, Ultrasensitive fluorescent proteins for imaging neuronal activity. *Nature* **499**, 295–300 (2013). doi: 10.1038/nature12354; pmid: 23868258

45. S.-B. Koh *et al.*, A quantitative FastFUCCI assay defines cell cycle dynamics at a single-cell level. *J. Cell Sci.* **130**, 512–520 (2017). doi: 10.1242/jcs.195164; pmid: 27888217

46. C. J. Cattin *et al.*, Mechanical control of mitotic progression in single animal cells. *Proc. Natl. Acad. Sci. U.S.A.* **112**, 11258–11263 (2015). doi: 10.1073/pnas.1502029112; pmid: 26305930

47. E. Fischer-Friedrich, A. A. Hyman, F. Jülicher, D. J. Müller, J. Helenius, Quantification of surface tension and internal pressure generated by single mitotic cells. *Sci. Rep.* **4**, 6213 (2014). doi: 10.1038/srep06213; pmid: 25169063

48. V. Rodionov, E. Nadezhdina, G. Borisy, Centrosomal control of microtubule dynamics. *Proc. Natl. Acad. Sci. U.S.A.* **96**, 115–120 (1999). doi: 10.1073/pnas.96.1.115; pmid: 9874781

49. D. Riendeau *et al.*, Arachidonyl trifluoromethyl ketone, a potent inhibitor of 85-kDa phospholipase A2, blocks production of arachidonate and 12-hydroxyeicosatetraenoic acid by calcium ionophore-challenged platelets. *J. Biol. Chem.* **269**, 15619–15624 (1994). pmid: 8195210

50. K. M. Dean, P. Roudot, E. S. Welf, G. Danuser, R. Fiolka, Deconvolution-free Subcellular Imaging with Axially Swept Light Sheet Microscopy. *Biophys. J.* **108**, 2807–2815 (2015). doi: 10.1016/j.bpj.2015.05.013; pmid: 26083920

51. M. Jacob, M. Unser, *IEEE Trans. Pattern Anal. Machine Intell* **26**, 1007–1019 (2004).

Science

The nucleus acts as a ruler tailoring cell responses to spatial constraints

A. J. LomakinC. J. CattinD. CuvelierZ. AlraiesM. MolinaG. P. F. NaderN. SrivastavaP. J. SáezJ. M. Garcia-ArcosI. Y. ZhitnyakA. BhargavaM. K. DriscollE. S. WelfR. FiolkaR. J. PetrieN. S. De SilvaJ. M. González-GranadoN. ManelA. M. Lennon-DuménilD. J. MüllerM. Piel

The nucleus makes the rules

Single cells continuously experience and react to mechanical challenges in three-dimensional tissues. Spatial constraints in dense tissues, physical activity, and injury all impose changes in cell shape. How cells can measure shape deformations to ensure correct tissue development and homeostasis remains largely unknown (see the Perspective by Shen and Niethammer). Working independently, Venturini *et al.* and Lomakin *et al.* now show that the nucleus can act as an intracellular ruler to measure cellular shape variations. The nuclear envelope provides a gauge of cell deformation and activates a mechanotransduction pathway that controls actomyosin contractility and migration plasticity. The cell nucleus thereby allows cells to adapt their behavior to the local tissue microenvironment.

Science, this issue p. eaba2644, p. eaba2894; see also p. 295

View the article online
https://www.science.org/doi/10.1126/science.aba2894
Permissions
https://www.science.org/help/reprints-and-permissions

Use of this article is subject to the Terms of service